

Supporting Information to: Fluorescence enhancement of single V2 centers in a 4H-SiC cavity antenna

Jonathan Körber,^{1,*} Jonah Heiler,^{1,2,3,*} Philipp Fuchs,⁴ Philipp Flad,⁵ Erik Hesselmeier,¹ Pierre Kuna,¹ Jawad Ul-Hassan,⁶ Wolfgang Knolle,⁷ Christoph Becher,⁴ Florian Kaiser,^{1,2,3} and Jörg Wrachtrup^{1,8}

¹3rd Institute of Physics, University of Stuttgart, Pfaffenwaldring 57, 70569 Stuttgart, Germany.

²Materials Research and Technology (MRT) Department,

Luxembourg Institute of Science and Technology (LIST), 4422 Belvaux, Luxembourg.

³Department of Physics and Materials Science, University of Luxembourg, 4422 Belvaux, Luxembourg

⁴Universität des Saarlandes, Fachrichtung Physik, Campus E2.6, 66123 Saarbrücken, Germany.

⁵4th Physics Institute and Research Center SCoPE,

University of Stuttgart, Pfaffenwaldring 57, 70569, Stuttgart, Germany.

⁶Department of Physics, Chemistry and Biology, Linköping University, 581 83 Linköping, Sweden.

⁷Leibniz-Institute of Surface Engineering (IOM), Permoserstraße 15, 04318 Leipzig, Germany.

⁸Max Planck Institute for Solid State Research, Heisenbergstraße 1, 70569 Stuttgart, Germany.

(Dated: July 2, 2024)

S1. METHODS

Structure optimization

To optimize the layer thicknesses of our design, we use a python code based on ref. [1]. We simulate the power emitted by a dipole within our structure into the solid angle that can be collected by an objective with $NA = 0.9$, normalized by the power emitted from a dipole in bulk silicon carbide into the same solid angle of the air objective. We choose a dipole orientation parallel to the interface since the sample is fabricated from a-plane silicon carbide, where the c-axis lies in the plane, and all V2 centers have a dipole parallel to the c-axis. The resulting photon collection factor is calculated for different wavelengths to estimate an overall collection enhancement by summing up the values weighted by the normalized V2-spectrum at the respective wavelength. For the optimization covering the



Figure S1: Light microscope images of the sample after membrane fabrication (before applying the silver coatings). (a) Microscope image of the full sample after the membrane fabrication. The 8 visible squares are the membrane regions. (b) Microscope image of the membrane that is used in the experiments. Color fringes arise due to a thickness gradient. The central part of the membrane is at a thickness of ~ 135 nm.

* These authors contributed equally to this work

full phonon side band, we do our calculations from 900–1150 nm with 5 nm wavelength steps. For the optimization in the other two spectral windows, we set the weighting factor to 0 for the wavelengths outside of the respective window.

Sample fabrication

The SiC sample for this study is cut from an n-type, a-plane 4H-SiC wafer (*Wolfspeed*) with a $\sim 10 \mu\text{m}$ -thick epilayer (free electron density of $\sim 7 \times 10^{13} \text{ cm}^{-3}$) grown on top by chemical vapor deposition. The creation of V2 centers and the fabrication of sub-micron thin membranes on our sample follows the steps from our previous work [2]. An image of the sample after the final thinning containing several membranes at different central thickness is shown in Figure S1. The outer framing of the sample still has a thickness of around $40 \mu\text{m}$, such that the sample can be moved with tweezers for cleaning and the subsequent coating steps. After identifying a membrane at the target thickness of $\sim 135 \text{ nm}$ (depicted in Figure S1 (b)), we apply a $\sim 200 \text{ nm}$ -thick silver layer by electron beam evaporation. Subsequently, we flip our sample and apply the thin silver layer by electron beam evaporation as well. As a last step, the SiO_2 layer is deposited to cover the thin silver layer, using ion-beam sputtering. We note that we do not break the vacuum between the thin-silver evaporation and the SiO_2 sputtering since both processes use the same vacuum chamber. In this way, the silver layer is covered even before its first contact with ambient conditions.

Room temperature confocal microscope setup

Our room temperature confocal microscope setup consists of a continuous-wave (CW) excitation laser with $\lambda = 785 \text{ nm}$ (*Cobolt 06-01, Hübner Photonics*). The laser is focused onto the sample with an objective (NA= 0.9) and the fluorescence is separated by the excitation with a dichroic mirror (*Semrock Di02-R830*). The collected fluorescence is then additionally filtered with a 900 nm longpass filter (*Thorlabs FELH900*), guided onto a polarizing beam splitter (PBS), coupled into two single-mode optical fibers (*Thorlabs 780 HP*) and guided onto SNSPDs (*PhotonSpot*). To address different positions on the sample, we scan our objective by piezo-actuators with a maximum range of $100 \mu\text{m} \times 100 \mu\text{m} \times 25 \mu\text{m}$.

ODMR measurements

To perform ODMR measurements on our sample at room temperature, we span a $50 \mu\text{m}$ -thick copper wire across the sample with a distance of $\sim 200 \mu\text{m}$ to the membrane center. We use a signal generator (*Rohde & Schwarz, SMIQ03*) and a microwave amplifier (*Mini Circuit LZY-22+*) to create a microwave sweep from typically 30–110 MHz with a power of typically 20–24 dBm sent through the wire after the amplifier. During the sweep, we detect fluorescence while continuously exciting the color center off-resonantly at 785 nm as a function of the microwave frequency in 1 MHz steps with an integration time of 50 ms for each point. Finally, we fit the acquired data using a double-Lorentzian function.

Autocorrelation measurements

For measuring the autocorrelation of the fluorescence, we make use of a standard Hanbury-Brown and Twiss (HBT) interferometer. To set an equal 50/50 ratio of photon counts between the two detectors, we adjust a $\lambda/2$ -waveplate in front of the PBS of our confocal setup, accordingly. For the correlation measurement, we use a timetagger (*Swabian Instruments*) and bin the detected correlations typically in 200 ps intervals. To analyze the data, we fit the autocorrelation measurements using a three level autocorrelation function for N single photon emitters [3]

$$\frac{1}{N} \cdot \left[1 - (1 + a) \cdot e^{-|\tau - \tau_0|/\tau_1} + a \cdot e^{-|\tau - \tau_0|/\tau_2} \right] + \frac{N - 1}{N}$$

where a , τ_0 and τ_1 are excitation power and intersystem crossing dependent parameters. From here, we extract the single photon purity as $g^{(2)}(\tau_0) = (N - 1)/N$. For background correction, we use the form [4]

$$g_{\text{corr}}^{(2)} = \frac{1}{\rho^2} [g_{\text{meas}}^{(2)} - (1 - \rho^2)]$$

with the background and emitter intensity dependent parameter $\rho = I_{em}/(I_{em} + I_{bg})$.

Saturation measurements

To extract the saturation count rate from single emitters, we measure the detected photon counts for different excitation power with the 785 nm laser. The given values of the excitation power are always measured directly before the objective. Each data point in a saturation measurement is the average of 100 measured count rates with each 100 ms integration time. As an error for each data point we use the standard deviation of the 100 measurements. To extract the saturation behavior, we fit the standard saturation curve with a linear term to include the background on each spot

$$I_{em}(P) = \frac{I_{sat} \cdot P}{P + P_{exc}} + b \cdot P. \quad (1)$$

using an orthogonal distance regression algorithm with python. We decide to include the background in the fit, since we find the background measured in close vicinity of individual spots strongly fluctuating for different regions even for regions very close to a specific emitter and thus does not give an accurate description of the background of each emitter. After the fit, we estimate the background corrected count values by correcting the measurements with the fit results.

Low temperature confocal microscope setup

For low temperature measurement, the sample is mounted inside a closed-cycle helium cooled cryostat (*Montana Instruments*) at ~ 8 K and emitters are addressed using a confocal setup with a NA=0.9, WD=1 mm, 100 \times objective (*Zeiss EC Epiplan-Neofluar*). The emitters are off-resonantly excited using a 728 nm laser (*Toptica iBeam-Smart-CD*) and the spectra are measured using a spectrometer (*Ocean Optics NIRQuest*). The frequency of the resonant excitation laser (*Toptica DL pro*) is recorded by a wavemeter (*HighFinesse Angstrom WS7-60*) and the resulting photons pass two tunable long pass filters (*Semrock TLP01-995*) with their edge tuned to ~ 925 nm for PSB detection before entering a single-mode fiber (*Thorlabs 1060 XP*) connected to the SNSPDs (*Photon Spot*).

PLE measurements

For the PLE measurements, we use the tunable laser in our low temperature confocal microscope setup. We apply a voltage ramp to the laser using a *National Instruments* data acquisition card (NIDAQ) and simultaneously record the laser frequency using a wavemeter (*HighFinesse Angstrom WS7-60*) as well as the photon counts in the PSB with our SNSPDs. For measurements on the reference sample, we drive the ground state spin transition continuously during PLE by applying a microwave signal (12–15 dBm input power), guided through a 50 μ m-thick wire to the emitter. For our measurements where we simultaneously scan two laser lines, we split the resonant laser into two paths and shift the optical frequency of both parts to a relative difference of 1 GHz using two acousto-optic modulators (*Gooch&Housego*).

Evaluation of PLE linewidths and spectral wandering

The PLE count rate is recorded over the voltage ramp that is applied to tune the resonant laser. In the first step of the evaluation, the voltage data is converted to frequencies using the data from the wavemeter for the respective ramp. A linear ramp between the minimum and maximum frequency recorded by the wavemeter is assumed for each PLE line which is in good agreement with the experimental data. Subsequently, the peaks in each PLE line are fitted using two Gaussian functions. To avoid corrupted fit data from lines with strong spectral jumping or ionization in between, a few constraints on the fit are employed. These constraints include peak positions in the scanning range, no negative amplitudes and offset, a linewidth bigger than one frequency step, an amplitude ratio below 10, a peak separation deviation below 40 %, and a general fit quality, determined by the r2 value, bigger than one of two thresholds 0.46 (0.7923). The power dependent mean linewidths are directly extracted from the fit data of all

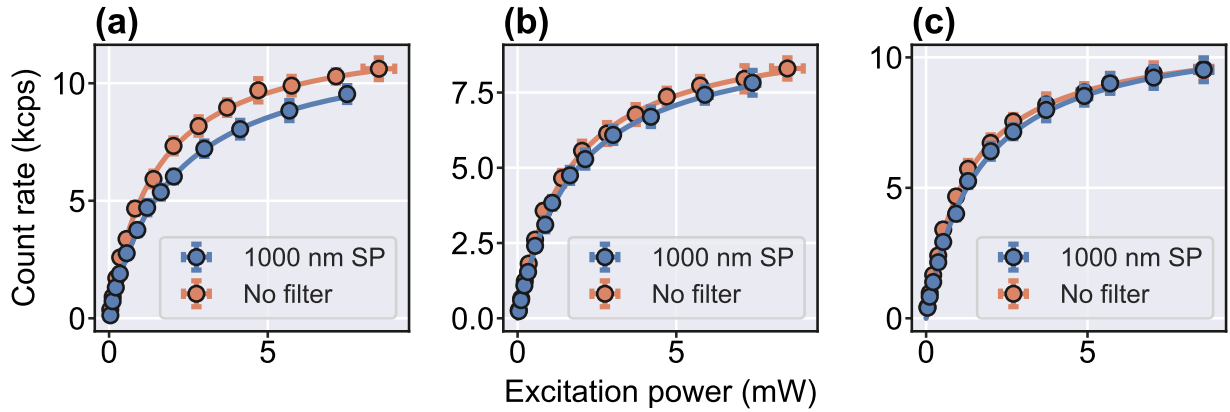


Figure S2: Saturation of 3 exemplary emitters at different filtering. Count rate under off-resonant excitation at the room temperature setup for three representative V2 centers from (a) to (c). The orange data sets are taken without filtering of the emission while for the blue data sets a 1000 nm shortpass filter was placed in the detection path. Solid lines show saturation fits on the datasets.

respective PLE measurement. The spectral wandering is calculated as the difference of the fitted A_2 peak position in two consecutive lines divided by the measurement time of one line.

S2. DETECTION EFFICIENCY OF THE ROOM TEMPERATURE SETUP

As stated in the main manuscript, the detection efficiency of our SNSPDs at the room temperature setup drops significantly for wavelengths larger than 1000 nm according to the spec sheets. To measure the influence on the detected photon count rate, we performed the saturation measurements of all emitters on the bulk reference samples for a second time with an additional 1000 nm shortpass filter (*Thorlabs FESH1000*) in the detection path. The measured saturation of 3 representative emitters are shown together with fits in Figure S2. Although the V2 emission ranges from ~ 917 –1100 nm with a significant amount above 1000 nm (see Figure 1(b) of the main manuscript), the saturation measurements only show a very small difference between the two filter settings. For all V2 emitters measured in the statistics of the main manuscript, the average saturation count rate yields 10.5 ± 1.4 kcps without an emission filtering (as used in the main manuscript) and 10.1 ± 1.7 kcps with the 1000 nm shortpass filtering. Therefore, the enhancement simulations in the main manuscript are always done for the spectral window of 900–1000 nm, comparable to the room temperature studies. For completeness and to understand the enhancement decrease at the low temperature setup, where a different SNSPD with a higher detection efficiency for wavelength above 1000 nm is used, we repeated the simulations for the different spectral windows in section S3.

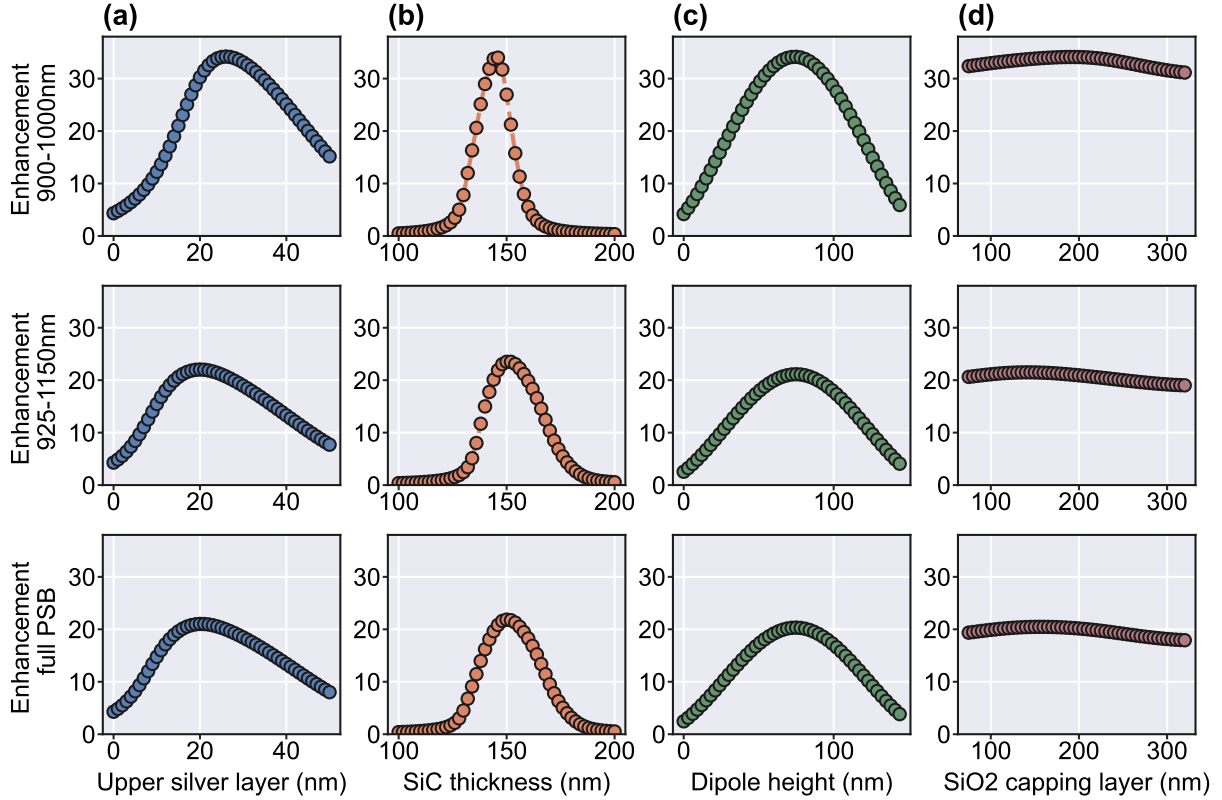


Figure S3: Enhancement as a function of the four relevant parameters. Simulated enhancement for different upper silver layer thickness (a), SiC thickness (b), height of the dipole with respect to the lower SiC-Ag interface (c), and thickness of the SiO₂ capping layer (d). For the upper row, the enhancement was simulated for collection of V2-emission in a spectral range from 900–1000 nm (as used in the RT measurements), for the central row in a spectral range from 925–1150 nm (as used in the LT measurements), and for the lower row for collection of the full PSB from 900–1150 nm.

S3. PARAMETERSWEEPS FOR THE FOUR RELEVANT LAYER THICKNESSES

To evaluate the effect of fabrication errors and different spectral detection windows to the enhancement of our structure, we extract the enhancement from the simulations explained in the methods section of the main text for different parameter sweeps. The enhancement is defined as the collected photon count rate of an emitter inside the structure divided by the count rate of a bulk emitter. Figure S3(a) to (d), respectively, show sweeps of the thickness of the upper silver layer, the thickness of the silicon carbide membrane, the height of the dipole emitter inside the membrane, and the thickness of the silica capping layer. For every parameter sweep, the three other parameters are kept at their optimum value. The different spectral detection windows are chosen to be 900–1000 nm, as used in the room temperature measurements, 925–1150 nm, as used in the low temperature measurements, and the full PSB 900–1150 nm for reference (see S3 from upper to lower row).

As stated in the main manuscript, variations in the silica layer do not change the photonic enhancement signif-

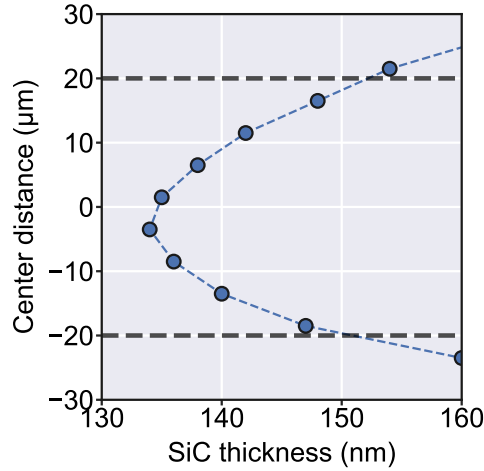


Figure S4: Thickness in the central part of the membrane. Membrane thickness for different vertical distance from the membrane center. The data is measured with the home-built WLI before the silver coating of the membrane. Black dashed lines enclose the vertical region around the membrane center with bright fluorescence from the main manuscript. The blue dashed line is a guide to the eye.

icantly and this layer is thus not critical in the fabrication. The most critical parameter to the enhancement is the thickness of the silicon carbide membrane, since it changes the resonance frequency of the structure. Here, the membrane has a thickness of ~ 135 nm at its central part, which is slightly below the optimum thickness. However, this is very beneficial for our case, since the membrane shows a thickness inhomogeneity and becomes thicker away from the center. The upper silver layer optimum is at a thickness of ~ 20 nm (~ 25 nm for 900–1000 nm), which we hit well in the fabrication. Since our sample is electron irradiated, V2 centers are created evenly distributed within the membrane and not only in the optimum dipole height which is roughly at the center of the membrane. Thus, the expected average enhancement in our case are smaller than the optimum values obtained from the simulations.

When we compare the enhancement for different spectral windows, the shape of the parameter variations remain almost unchanged but the overall enhancement changes. This is mainly due to the fact that our resonance is narrower than the PSB, meaning that it does not yield an enhancement in the outer parts of the side band, thus, decreasing the average enhancement when measuring the full PSB. For our room temperature measurements, we are not able to measure the full PSB, since the efficiency of the detectors drops significantly for wavelengths above 1000 nm. When using the structure with a detection system that covers the full spectral bandwidth of the PSB, the enhancement is lowered by a factor of ~ 0.65 , yielding an expected enhancement of $\times 22$ for the optimum case instead of $\times 34$. In our low temperature measurements, we use different detectors with a much higher detection efficiency above 1000 nm but we limit our detection window to 925–1150 nm since the ZPL needs to be filtered in emission to avoid laser counts from the resonant excitation. As shown in the last row of Figure S3, the enhancement in this case is lowered by a factor of ~ 0.7 .

S4. MEMBRANE THICKNESS OF THE REGION WITH INCREASED FLUORESCENCE

In our room temperature confocal measurements, we have found a big, circular area with bright fluorescence in the center of the antenna, shown in Figure 2(a) of the main manuscript. The diameter of this region is around $40 \mu\text{m}$. Measurements with our home-built WLI, taken before the silver coating, are depicted in Figure S4. They show a minimum thickness of 134 nm and a maximum thickness of 153 nm. As discussed in the main text, the simulation shows the maximum enhancement for a membrane thickness between 135–155 nm, thus, matching our experiments.

S5. REFERENCE BULK AND SIL SAMPLES FOR THIS STUDY

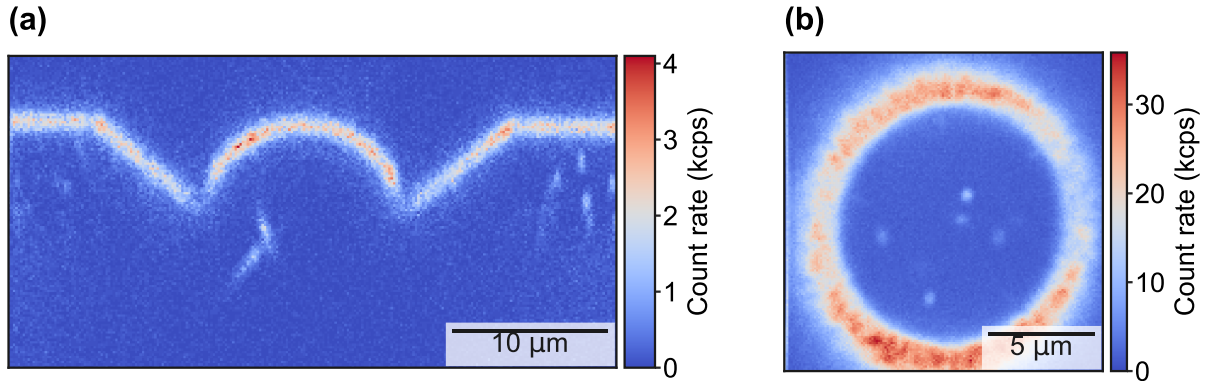


Figure S5: Confocal scan of a SIL on the reference sample. (a) XZ-scan of a SIL fabricated on the reference sample under $100\ \mu\text{W}$ excitation with the 785 nm laser. The y-position is fixed to the center of the SIL. The cross-section of the SIL surface is visible in the upper part of the image. In the lower part one can see single emitters in the SIL as well as in the bulk part next to the SIL. (b) XY-scan of the SIL with $90\ \mu\text{W}$ excitation (785 nm) at a z position a couple of μm deep in the SIL. Several, single emitters are visible in the scan.

The samples used for the reference measurements are fabricated from the same starting material, i.e., n-type 4H-SiC wafer with a $\sim 10\ \mu\text{m}$ -thick epilayer. The reference sample from Figure 2(b) of the main manuscript has been irradiated with the same dose of 5 kGy as the main sample. The second reference sample, used for the bulk and SIL reference measurement for the room temperature enhancement, has been irradiated with a dose of 2 kGy. Eight SILs with a diameter of $10\ \mu\text{m}$ were fabricated using focused-ion-beam (FIB) milling with a gallium beam. Figure S5 shows confocal scans of such a created SIL. For the bulk measurements, a region $\sim 50\ \mu\text{m}$ next to a SIL was used. The last reference sample, used for measuring the spectral distribution of the A2 position in 40 SIL emitters, is made of the same starting material but has been irradiated with a dose of 20 kGy before the SIL fabrication.

S6. ODMR FOR DIFFERENT SAMPLES AT THE ROOM TEMPERATURE SETUP

As stated in the main manuscript, our room temperature ODMR measurements on V2 centers show two peaks. To exclude effects introduced by our optical structure as the origin, we measured ODMR for V2 centers on different samples in addition. Figure S6 shows ODMR measurements for three different samples, each with two peaks centered around 70 MHz. The splittings extracted from the fits are $11.6 \pm 0.4\ \text{MHz}$, $10.0 \pm 0.3\ \text{MHz}$, and $9.8 \pm 0.3\ \text{MHz}$ from left to right. Since the splittings are in the same range (between 9–13 MHz for all the investigated emitters) we conclude that our setup has a magnetized part very close to the sample (most likely the objective) which creates the splitting by a magnetic field of $\sim 3\text{--}5\ \text{Gauss}$ parallel to the c-axis [5].

S7. POLARIZATION BASED PRESELECTION OF BRIGHT CONFOCAL SPOTS

To find a high number of V2 centers within the bright spots in our antenna sample without the need of doing an ODMR measurement for all of them, we make use of our polarization dependent collection path. As depicted in Figure S7(a), we place a $\lambda/2$ -waveplate in front of a polarizing beam splitter (PBS) in our detection beam and send the two outputs of the PBS on an SNSPD. We originally implemented this setup to be able to tune a 50/50 illumination of both SNSPDs for the autocorrelation measurements. However, we can also use it to detect candidates for V_{Si} centers in 4H-SiC since their dipole emission is always oriented along the c-axis of the crystal [6]. To do so, we use the emission from a spot that shows a very clear ODMR peak as a calibration and rotate the $\lambda/2$ -waveplate to set an almost perfect 50/50 ratio on both detectors. This setting is then fixed for further measurements. When the

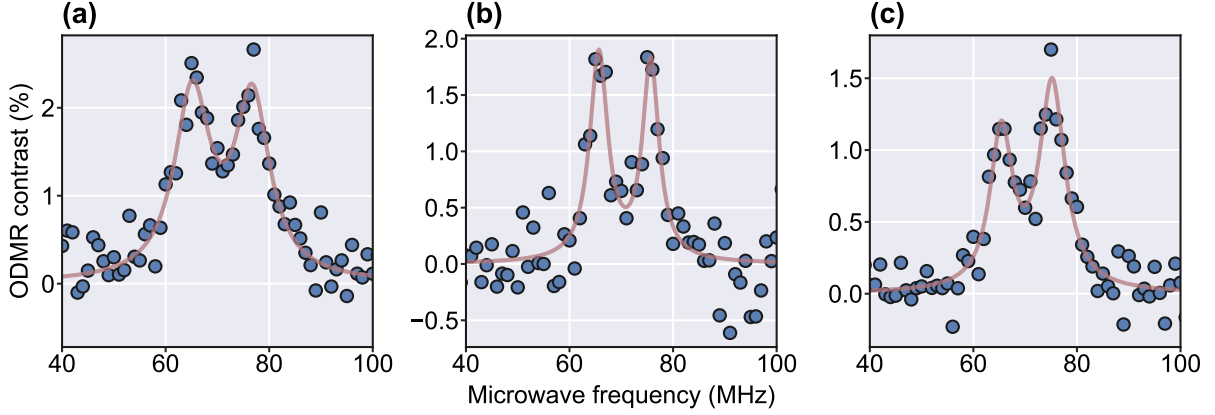


Figure S6: ODMR measurements on single V2 emitters of three different samples. ODMR measurements of a single V2 emitter on the antenna sample **(a)**, the reference SIL sample **(b)**, and a third, different sample **(c)**. The solid red lines show double-Lorentzian fits to the data.

dominant emission contribution of a bright spot on a different position originates from a V_{Si} , the polarization and thus the count rate ratio of both detectors should not change, as shown in a time trace measurement of photon count rates for 100 ms integration time in Figure S7(b). For other spots, however, this ratio can differ quite significantly from the initially set 50/50 ratio, as shown in Figure S7(c), indicating that the collected fluorescence does not come from a V_{Si} center. To quantify this effect, we define the polarization deviation ΔPol using the measured count rate of detector 1 (Pol1) and detector 2 (Pol2) for N time traces

$$\Delta\text{Pol} = \frac{100}{N} \sum_N \left(\frac{1}{2} - \frac{\text{Pol1}}{\text{Pol1} + \text{Pol2}} \right).$$

The polarization deviation of the two shown examples are $\Delta\text{Pol} = 0.91\%$ for Figure S7(b) and $\Delta\text{Pol} = 14.16\%$ for Figure S7(c). A the perfect value of $\Delta\text{Pol} = 0\%$ cannot be reached in the experiment since the $\lambda/2$ -plate being turned by hand and due to the influence of shot noise in the photon detection. We use this preselection and only consider spots with $\Delta\text{Pol} < 1.5\%$ for further investigations with ODMR measurements in the room temperature study.

Using this preselection, we increase the relative amount of V2 centers from the 18.8% in the antenna sample to 45%. Note that this is in good agreement with the expectation of roughly 50%, as both the V2 and the V1 center are found with our preselection method and we expect to create those color centers with similar probability during the electron irradiation.

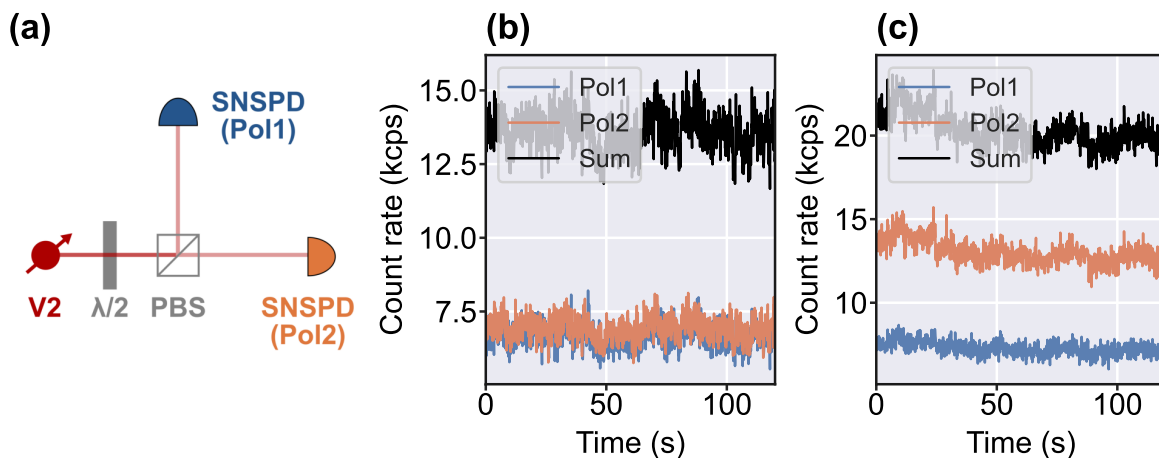


Figure S7: Polarization of the collected emission from bright spots. (a) Schematic of the detection path in our room temperature confocal setup. The emitted light passes a $\lambda/2$ -waveplate and is directed onto a polarizing beam-splitter (PBS), that splits the beam into two paths, both sent to an SNSPD. (b) Recorded time trace of photon count rates of a V2 emitter. The orange (blue) curve shows the time trace of the SNSPD for horizontal (vertical) polarization and the black curve shows the sum of the two. (c) Recorded photon count rate trace of a bright spot that is not a V2 emitter with the same $\lambda/2$ setting as in (b). The polarization of the emission has significantly changed compared to (b).

S8. AUTOCORRELATION VALUES FOR ALL MEASURED EMITTERS

Figure S8 shows the fitted saturation count rate over the fitted autocorrelation at zero time delay for all V2 emitters of our room temperature study before (blue) and after (orange) applying a background correction for the autocorrelation fit. This correction is based on the fitted background from the corresponding saturation study. For the bulk emitters in Figure S8(a), only six representative emitters of the 40 emitters from the statistics were investigated since autocorrelation measurements take a lot of time to yield a reasonable signal to noise ratio at the low photon count levels of bulk emitters. Considering only the 14 antenna emitters with an anti-bunching drop below 0.5 without background correction yields an average enhancement of $\times (9.4 \pm 2.6)$ and a maximum enhancement of $\times (12.5 \pm 1.8)$, which is very similar to the statistics including all emitters after background correction as presented in the main manuscript.

S9. PLE CATEGORIES OF THE ANTENNA EMITTER

To find emitters at low temperature for measuring PLE, we take emission spectra of bright spots on our sample and investigate spots with a clear peak around the V2 ZPL of ~ 917 nm. We consider all spots that show an emission peak in the range of 916.2–918.2 nm for subsequent PLE measurements, since this range was found to be accessible by tuning the grating of our resonant laser. Our PLE measurements show emitters that can be assigned to one of three categories: 1.) emitters that show two, clearly distinguished absorption lines, 2.) emitters with a very broad absorption linewidth such that the two lines can hardly be distinguished, and 3.) emitters where only occasional blinking but no stable lines are observed at all. Figure S9 shows the spectra (upper row) and a series of PLE lines (lower row) for three exemplary emitters of these categories.

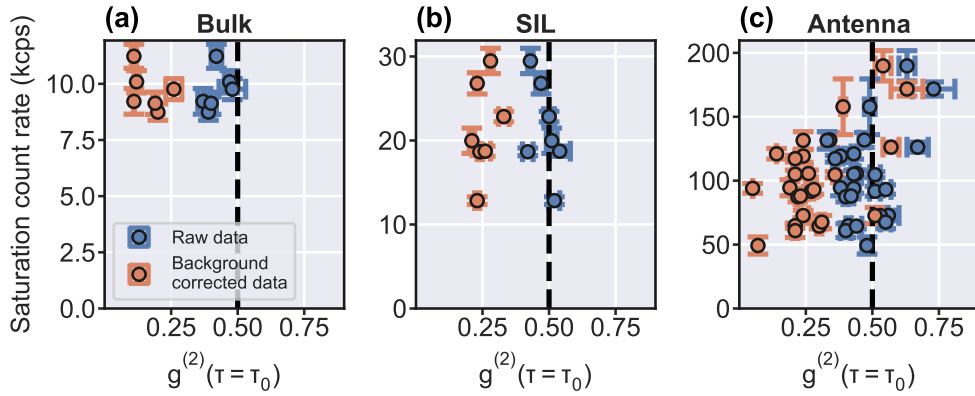


Figure S8: Saturation count rates and autocorrelation drops at zero time delay. (a) Saturation count rate plotted over the fitted value of the autocorrelation measurement dip at zero time delay for representative V2 emitters in the bulk before (blue) and after (orange) background correction. The same depiction is shown in (b) for all checked V2 emitters in the SIL sample and in (c) for all measured V2 emitters in the antenna sample. The error bars in x (y) are the standard deviations from the corresponding saturation (autocorrelation) fits. Black, dashed lines indicate the single-emitter threshold of $g^{(2)}(0) = 0.5$

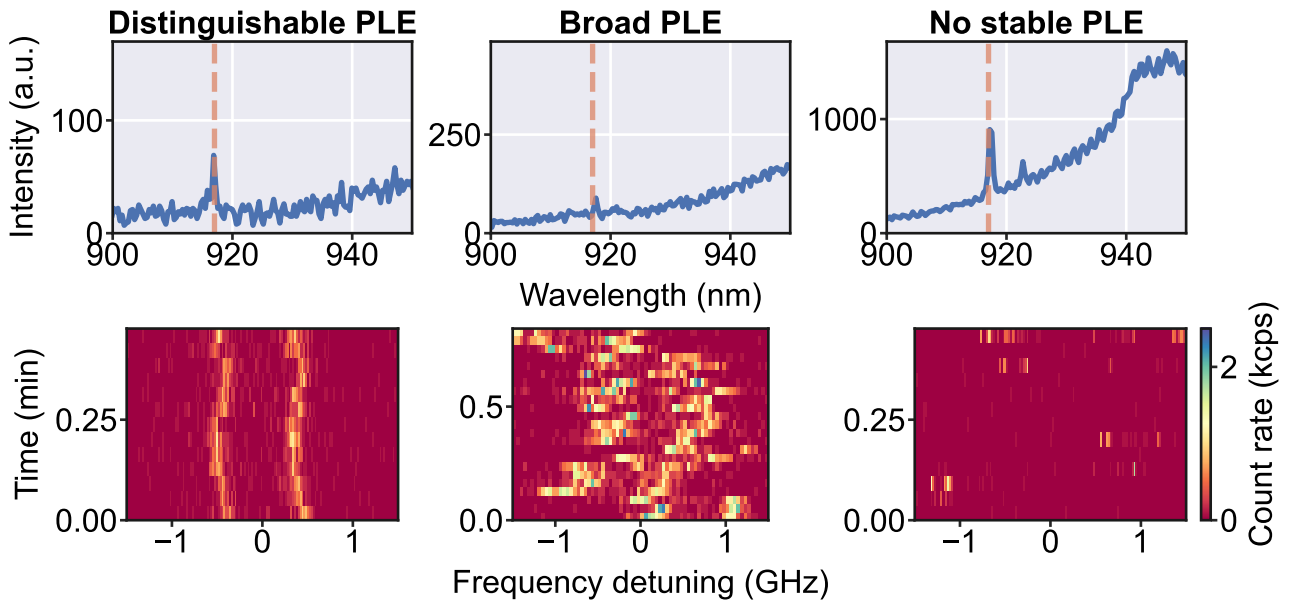


Figure S9: Low-temperature emission spectra and PLE of V2 centers in the antenna sample. (Upper row): Emission spectra under off-resonant excitation (blue). Orange, dashed lines indicate the position of the V2 ZPL for bulk samples. **(Lower row):** PLE for the spots with respective emission spectrum in the upper row.

S10. BRIGHTNESS OF ANTENNA EMITTERS AT RESONANT EXCITATION

As we discuss in the main manuscript, we extract the enhancement of the structure under resonant excitation through power dependent double-laser PLE measurements for 3 emitters in the bulk, 3 in the SIL, and 10 emitters in the antenna sample. For all emitters, we measure 10 PLE lines for each excitation power and stop the measurement at the excitation power where we ionize the emitter regularly after 1-2 lines. At next, we fit each single PLE line using a Gaussian and consider only fit results with a r^2 -value of 0.8 or higher to discard spectrally unstable lines or lines that

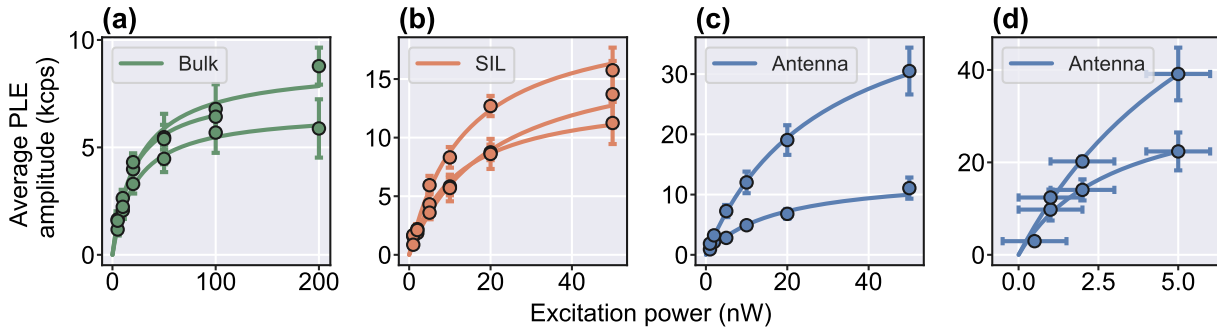


Figure S10: Saturation count rates under resonant excitation. Count rates under resonant excitation extracted from the amplitudes of Gaussian fits on the PLE lines for 3 emitters in the bulk (a), 3 in the SIL (b), and 4 emitters in the antenna sample (c) and (d). Solid lines are saturation fits to the data. The y-error bars in the data points are the standard deviation of the amplitude fits of the PLE lines. Due to the significantly different saturation powers, the results from the four emitters of the antenna in (c) and (d) are plotted separately.

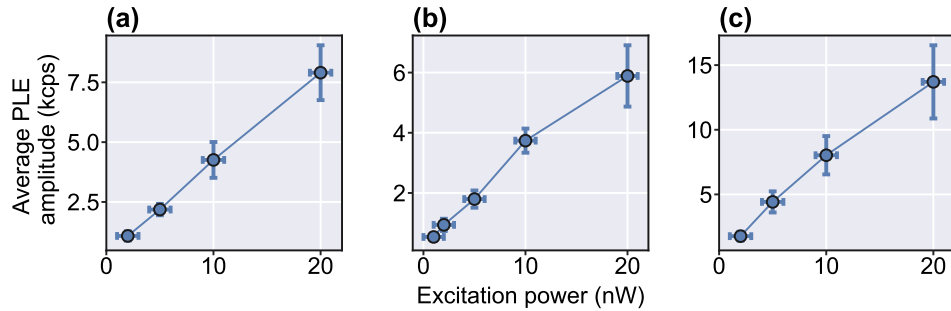


Figure S11: Excitation power dependent count rates without saturation. Count rate as a function of resonant excitation power for 3 different emitters (a) - (c) in the antenna sample. The solid line is a guide to the eye that underlines that for all three cases no saturation is visible yet.

ionize already during the PLE measurement. For each emitter, we plot the average fitted amplitude as a function of the excitation power and fit the data with a saturation curve, as for our room temperature study. Here, we neglect the linear term in the saturation that accounts for the background, since background counts are highly suppressed at resonant excitation.

The results are depicted in Figure S10 for the 3 bulk and SIL emitters as well as for 4 emitters from the antenna sample where the saturation power could be confidently extracted. The emitters from the antenna sample are shown in the two plots S10(c) and (d), since they show a big difference in the maximum excitation power just before ionization. We believe that this is a result of different power levels that emitters close to (away from) the membrane center experience at the same excitation power due to the cavity resonance being closer to (further from) 917 nm. The average saturation count rates for the three cases are 7.8 ± 0.9 kcps (bulk), 17.4 ± 2.9 kcps (SIL) and 48.2 ± 30.2 kcps (antenna). Note, that especially for the antenna emitters the saturation count values fluctuate strongly between different emitters. The resulting enhancement factors for the SIL and antenna are $\times (2.23 \pm 0.45)$ and $\times (6.18 \pm 3.94)$, respectively. Apart from the emitter placement that plays a role for the enhancement in the antenna, we can attribute the fluctuation to missing data points in the saturated regime. We could not record these points due to earlier ionization and even find emitters in the antenna where no saturation at all can be observed in the non-ionizing power range. Three examples of this case are shown in Figure S11.

-
- [1] Philipp Fuchs, Software for "Theoretische und praktische Implementierung nanophotonischer Strukturen in Diamant" (2021). <https://zenodo.org/records/5556435>.
 - [2] J. Heiler, J. Körber, E. Hesselmeier, P. Kuna, R. Stöhr, P. Fuchs, M. Ghezellou, J. Ul-Hassan, W. Knolle, C. Becher, F. Kaiser, and J. Wrachtrup, Spectral stability of V2 centres in sub-micron 4H-SiC membranes, *npj Quantum Mater.* **9** (2024).
 - [3] F. Fuchs, B. Stender, M. Trupke, D. Simin, J. Pflaum, V. Dyakonov, and G. V. Astakhov, Engineering near-infrared single-photon emitters with optically active spins in ultrapure silicon carbide, *Nat. Commun.* **6**, 7578 (2015).
 - [4] R. E. Fishman, R. N. Patel, D. A. Hopper, T. Y. Huang, and L. C. Bassett, Photon-Emission-Correlation Spectroscopy as an Analytical Tool for Solid-State Quantum Defects, *PRX Quantum* **4**, 010202 (2023).
 - [5] H. Kraus, V. A. Soltamov, F. Fuchs, D. Simin, A. Sperlich, P. G. Baranov, G. V. Astakhov, and V. Dyakonov, Magnetic field and temperature sensing with atomic-scale spin defects in silicon carbide, *Sci. Rep.* **4**, 5303 (2014).
 - [6] E. Janzén, A. Gali, P. Carlsson, A. Gällström, B. Magnusson, and N. T. Son, The silicon vacancy in SiC, *Phys. Rev. B Condens.* **404**, 4354 (2009).